The Astrophysical Journal, 783:104 (13pp), 2014 March 10 doi:10.1088/0004-637X/783/2/104

FIRST FAINT DUAL-FIELD OFF-AXIS OBSERVATIONS IN OPTICAL LONG BASELINE INTERFEROMETRY

J. Woillez[1,2], P. Wizinowich[1], R. Akeson[3], M. Colavita[4], J. Eisner[5],
R. Millan-Gabet[3], J. D. Monnier[6], J.-U. Pott[7], and S. Ragland[1]
[1] W. M. Keck Observatory, Kamuela, HI 96743, USA
[2] European Southern Observatory, Karl-Schwarzschild-Strasse 2, Garching bei Mnchen, D-85748, Germany
[3] NASA Exoplanet Science Institute, California Institute of Technology, Pasadena, CA 91125, USA
[4] Jet Propulsion Laboratory, California Institute of Technology, Pasadena, CA 91109, USA
[5] University of Arizona, Tucson, AZ 85721-0065, USA
[6] University of Michigan, Ann Arbor, MI 48109-1090, USA
[7] Max-Planck-Institut für Astronomie, Heidelberg, D-69117, Germany
Received 2013 July 19; accepted 2014 January 24; published 2014 February 20

ABSTRACT

Ground-based long baseline interferometers have long been limited in sensitivity in part by the short integration periods imposed by atmospheric turbulence. The first observation fainter than this limit was performed on 2011 January 22 when the Keck Interferometer observed a $K = 11.5$ target, about 1 mag fainter than its $K = 10.3$ atmospherically imposed limit; the currently demonstrated limit is $K = 12.5$. These observations were made possible by the Dual-Field Phase-Referencing (DFPR) instrument, part of the NSF-funded ASTrometry and phase-Referenced Astronomy project; integration times longer than the turbulence time scale are made possible by its ability to simultaneously measure the real-time effects of the atmosphere on a nearby bright guide star and correct for it on the faint target. We present the implementation of DFPR on the Keck Interferometer. Then, we detail its on-sky performance focusing on the accuracy of the turbulence correction and the resulting fringe contrast stability.

Key words: instrumentation: high angular resolution – instrumentation: interferometers

Online-only material: color figures

1. INTRODUCTION

One of the fundamental limitations of a ground-based optical long-baseline interferometer is the turbulent atmosphere; its coherence time $T_{0,2}$ (Buscher 1994; two apertures and interval variance definition) sets the maximum integration time for an interferometric measurement. The same limit for single telescope instruments has been overcome by means of adaptive optics (AO): a wavefront sensor measures the turbulence faster than its evolution timescale and corrects for it with a deformable mirror (DM), making longer integrations possible at the diffraction limit. Fringe trackers are the equivalent of AO on an interferometer: fringe sensors measure the atmospheric turbulence differential piston affecting the interference fringe's position between pairs of telescopes and correct for it with delay lines, as first demonstrated by Shao & Staelin (1980).

Whereas fringe trackers have already been used on optical interferometers to observe bright objects at higher spectral resolution (AMBER and FINITO: Le Bouquin et al. 2008; ASTrometry and phase-Referenced Astronomy (ASTRA) self phase referencing: Woillez et al. 2012; Pott et al. 2010), to increase the precision of existing measurements affected by thermal background (Keck Nuller: Colavita et al. 2009; MIDI and PRIMA Fringe Sensor Unit: Müller et al. 2010; Pott et al. 2012), to observe objects at a low fringe contrast (Monnier et al. 2012), or increase the astrometric precision measured for narrow binaries (Lane & Muterspaugh 2004), this article focuses on the sensitivity improvement they can provide beyond the turbulence limit. The observation configuration considered here and described with a narrow-angle astrometry emphasis in Shao & Colavita (1992), is that of a fringe tracker measuring the atmospheric turbulence from a bright reference target providing a correction to a nearby faint target, which is itself observed at integration times longer than the turbulence timescale. Following the single-telescope analogy, this is exactly the configuration of an off-axis AO system. This observation technique, dual-field off-axis fringe-tracking, was pioneered at the Palomar Testbed Interferometer (Colavita et al. 1999), aiming for a demonstration of narrow-angle astrometry on bright pairs. Its performance was investigated on bright pairs (Lane & Colavita 2003; Lane 2003), but always within this interferometer on-axis limiting magnitude.

On UT 2011 January 22, the Keck Interferometer locked its bright reference fringe tracker, which was running at a 4 ms integration period, on TYC 5322-154-1, a $K = 7$ mag on-axis star, and provided a correction for a fainter off-axis star *2MASS J04531720−0755503*, which is 10 arcsec away. Using a 0.1 s integration period, the faint science fringe tracker was able to follow fringes and measure an uncalibrated contrast of 0.89 on this $K = 11.45$ mag unresolved star, which is 1 mag beyond the interferometer's atmospherically limited magnitude of $K = 10.3$ mag. This was the first time a long-baseline optical interferometer managed to observe an object fainter than its turbulence limit using dual-field off-axis fringe tracking. At the time of this writing, the sensitivity had been demonstrated to $K = 12.5$, on *2MASS 17342850+0319454*, with the $K = 7$ reference target *TYC 418-1965-1* at a separation of 10 arcsec.

Section 2 of this article details the implementation of the Dual-Field Phase-Referencing[8] (DFPR) instrument, carried-out under the NSF-funded ASTRA project (Woillez et al. 2010).

[8] Dual-Field Phase-Referencing should be understood as the name of the instrument, a part of the ASTRA project, where the bright reference object is used to stabilize the phase of the faint object in order to perform visibility measurements on it. It does not refer to phase-referenced imaging as described in Delplancke (2008) for PRIMA. Phase-referenced imaging of a resolved object has a baseline knowledge requirement as strong as astrometry (Woillez & Lacour 2013). As such it would have been possible, on the Keck Interferometer, only after the implementation of the astrometric phase of the project.

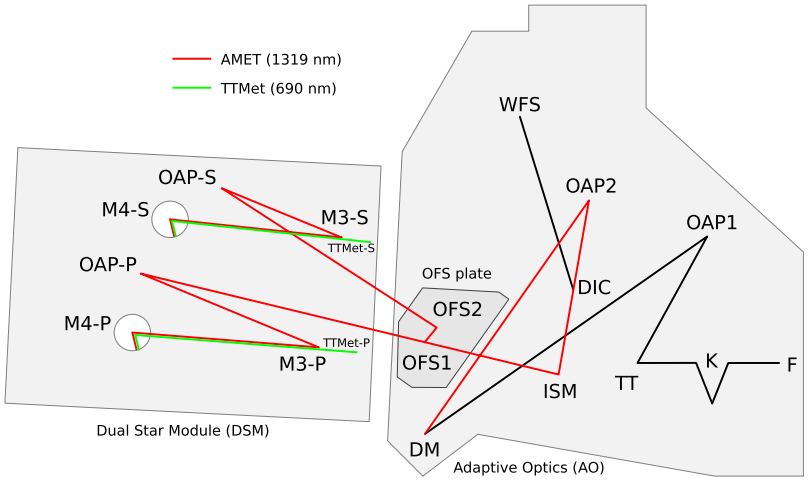

Figure 1. Layout of the dual star module (DSM) and Keck adaptive optics (AO) system, located inside the AO enclosure on the left Nasmyth platform of the telescopes. F: telescope focus; K: K-mirror rotator; TT: tip/tilt mirror; OAP1: collimating off-axis parabola; DM: deformable mirror; OAP2: focusing off-axis parabola; DIC: IR-transmissive dichroic; WFS: wavefront sensor area; ISM: interferometer science fold mirror; OFS1 and OFS2: first off-axis selector mirror at AO focus and second off-axis field selector mirror, both located on removable OFS plate; OAP-P and OAP-S: primary and secondary recollimating off-axis parabola; M3-P and M3-S: primary and secondary M3 dichroics; M4-P and M4-S: primary and secondary M4 fold mirrors; TTMet-P and TTMet-S: primary and secondary tip/tilt metrology source plates, injected through M3 dichroics. The AMET metrologies for the primary and secondary are terminated to a common point in front of the deformable mirror (DM).

(A color version of this figure is available in the online journal.)

Section 3 presents the demonstrated off-axis fringe-tracking and visibility measurement performance measured on bright–bright and bright–faint pairs.

2. IMPLEMENTATION

The implementation of the DFPR instrument on the Keck Interferometer is an evolution of the Self-Phase-Referencing instrument described in Woillez et al. (2012), and relies on many aspects of the infrastructure developed for NASA's Keck Interferometer project (Colavita et al. 2013). Therefore, the details given in this section focus on the additions specific to the dual-field aspect and its application to faint object observations: the *dual-field subsystem* (Section 2.1), which separates the bright reference from the faint science object, stabilizing them on the fast fringe tracker and focal instrument, respectively; the *internal optical path control* (Section 2.2), which actively compensates the instrumental optical path difference (OPD) fluctuations for each of the bright and faint objects; and finally the *phase-referencing architecture* (Section 2.3), which is responsible for measuring the residual OPD fluctuations of instrumental and atmospheric origins of the bright reference object and applying an appropriate correction to the faint science object.

Since the ASTRA project also aimed to provide a narrow-angle astrometry (Shao & Colavita 1992) capability, some aspects of the components detailed below are more relevant to this unfinished capability than to DFPR. They are, however, mentioned for future reference.

2.1. Dual-field Subsystem

2.1.1. Dual Star Module

The dual star modules (DSMs; Figure 1) are at the interface between the Keck AO systems (Keck AO; Wizinowich et al. 2000, 2006) and the interferometer coudé trains (Colavita et al. 2013). Their purpose is to select two independent fields at each telescope within the Keck AO field of view and deliver them via the primary and secondary beam trains to the interferometric basement where OPD compensation and beam combination are performed.

The key component is the off-axis field selector (OFS), located on a removable platform installed on the AO bench, at an output focus of the AO system delivered by the interferometer science mirror. The OFS consists of a pair of steering mirrors (OFS1 and OFS2) acting as a periscope. A 1.5 arcsec radius hole, at the center of OFS1, transmits a primary on-axis field to the primary beam train. The pair of OFS mirrors reflects a secondary field, between 3 and 30 arcsec off-axis[9], by sending it to the secondary beam train. After the OFS, both primary and secondary diverging beams are recollimated with off-axis parabolas (OAP-P and OAP-S) and are sent through the primary and secondary beam trains (both already used by the Keck Nuller instrument; Colavita et al. 2009) to the interferometric basement.

The OFS stays fixed throughout an observation, but moves at acquisition time to match the position of the off-axis object within the stable field delivered by the AO system. This requires that the AO system be run in position angle mode, where the K-mirror rotator (noted K in Figure 1) compensates the field rotation at the Nasmyth focus of a Keck telescope. The position of the OFS mirrors is computed based on the position of the off-axis target relative to the on-axis target. For each new relative off-axis position requested, the OFS pointing code avoids sending the secondary field through the central hole of the annular mirror in order to prevent breaks in the longitudinal metrology.[10]

2.1.2. Acquisition of Fields

The acquisition of a pair of reference and science targets for the interferometer involves a combination of telescope,

[9] The minimum separation of 3 arcsec is conservatively deduced from the primary field aligned at the center of the OFS annular mirror, and the secondary field located at twice the radius of the annular mirror circular hole. This minimum separation could be reduced by moving both primary and secondary fields closer to the edges of the hole.

[10] This was not necessary for off-axis fringe tracking, but was implemented for astrometry.

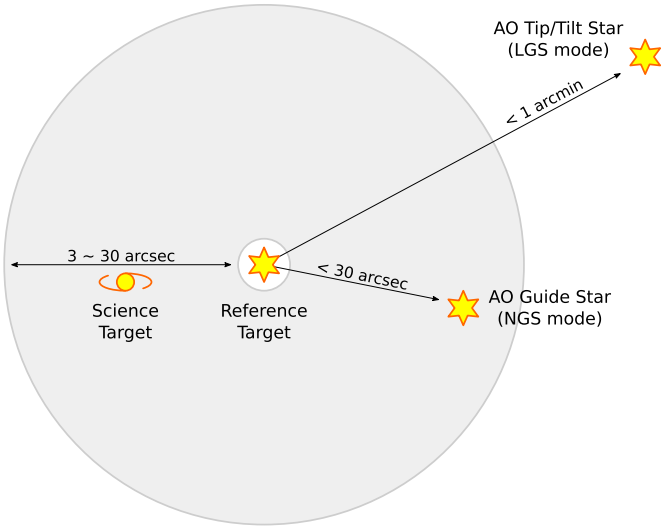

Figure 2. Acquisition field of view. When observing with Dual-Field Phase-Referencing, the interferometer reference target is typically on-axis, and the science target is 3–30 arcsec off-axis. When the adaptive optics (AO) operates in Natural Guide Star (NGS) mode, the AO guide star can be up to 30 arcsec away from the optical axis; when in Laser Guide Star (LGS) mode, the AO tip Tilt star can be up to 1 arcmin away from the optical axis, and the LGS is typically kept on the interferometer reference target. The entire field can be shifted with a telescope offset to send the science target to the primary beam train, as long as the AO constraints are still respected.

(A color version of this figure is available in the online journal.)

AO, and OFS offsets. When the AO is operated in Natural Guide Star (NGS) mode, the AO loops are first closed on-axis on the AO guide star (AO-NGS). If the reference target (Ref) of the interferometer is different from the AO-NGS, both the telescope and AO are offset up to 30 arcsec to bring the reference target on-axis for the primary beam train. When the AO is operated in Laser Guide Star (LGS) mode, the AO tip/tilt and DM loops are closed on the tip/tilt star (AO-TT) and laser guide star (AO-LGS), both of which are initially on-axis. Then the telescope and the tip/tilt part of the AO are offset to the interferometer reference star up to 1 arcmin away. The LGS, kept on-axis, is aligned with the interferometer reference star and provides the best AO correction there. In both cases, the interferometer science target (Sci) is acquired with an OFS offset in the 3–30 arcsec range mentioned earlier. All acquisition limits are illustrated in Figure 2.

These acquisition operations are fully automated with a combination of the AO acquisition widget (Le Mignant et al. 2006), and the interferometer sequencer (Colavita et al. 2013). In addition, the sequencer is capable of permuting which of the Sci and Ref targets is sent into the primary and secondary beam trains. This functionality was originally planned for astrometry where regular swaps are needed to calibrate the zero point of the astrometric metrology, but is used in dual-field to quickly find the fringe position for the secondary beam train using the brighter reference target in addition to finding the fringe position for the primary beam train itself.

The OFS has not been designed with high pointing precision or accuracy in mind, and the beam trains after the field separation have moving parts. Therefore, it is not possible to blindly position on the sky the fringe tracker fibers with the separation of the observed pair. This is addressed by measuring the current differential pointing of the primary and secondary beam trains with the AO acquisition camera: the visible alignment lasers of the interferometer, launched from the beam combiners, reflect off the metrology corner cube in front of the AO DM and reach this acquisition camera. This beam train differential pointing direction information, measured in the common path before the field separation, can then be used to apply corrections to the OFS.

2.1.3. Tip/Tilt Control

Most of the atmospheric and some of the telescope tip/tilt is corrected by the Keck AO systems. The additional tip/tilt, introduced after the AO system by the non-evacuated beam trains, is corrected by an *H*-band angle tracker. This angle tracker is based on a single infrared detector, traditionally running at 80 Hz on bright ($H < 10.5$) objects, where up to four star positions can be stabilized, matching the four beam trains delivered by the Keck telescopes. When observing fainter objects, the camera has to be slowed down to reach the magnitude of the faint object found in one of the two beam trains. The achieved correction bandwidth can then only address very slow drifts of thermal or alignment origin, leaving tip/tilt vibrations and beam train turbulence uncorrected. Ideally, one would want a dedicated slow camera for the faint object and keep a fast rate on the bright object. An intermediate solution was implemented with the addition of a variable length average filter on the image data stream coming from the camera, before the centroid processing. Increasing the length of the filter is a less readout-noise-efficient equivalent to slowing down the camera. This approach keeps a good tip/tilt control bandwidth on the bright object where the average filter is disabled and is necessary to achieve proper fringe tracking. A better approach requiring only one camera would have been to either remove the destructive reads for the regions of interests containing the faint object, or to equip one of the three unused detector quadrants with an additional readout electronic and run two quadrants at two different rates.

An internal tip/tilt metrology system was initially planned for the DFPR to recover some of the lost control bandwidth on the faint angle tracker and to potentially improve the correction for the bright object. It consisted of a 690 nm laser beacon injected in the four beam trains after the field selections (at M3 in Figure 1), and two-dimensional position sensing devices (PSD) located in the basement next to the infrared angle trackers (see Section 2.1.3). The PSDs were supposed to measure any tip/tilt introduced by the beam trains after the AO correction, and send a fast correction to the existing tip/tilt mirror in the interferometric basement. Such a system would have preserved the tip/tilt stability delivered by the AO systems down to the interferometric basement and would have been able to work in parallel with the angle tracker. However, the implementation never worked properly: the low transmission to the PSDs at 690 nm required operating the beacons at a power level high enough to contaminate the AO wavefront sensors; this component was therefore never successfully used on the sky. A fix, which has not been implemented, would have been to relocate the tip/tilt metrology sensors before the fringe tracker pick-up dichroics, which are responsible for most of the tip/tilt metrology transmission issue, either as part of the AMET dichroic (see Astrometric METtrology in Figure 3), or as dedicated 690 nm pickup dichroics.

2.2. Internal Optical Path Control

The Keck Interferometer is equipped with a network of sensors responsible for minimizing the OPD fluctuations caused by the instrument. For the DFPR instrument, they not only

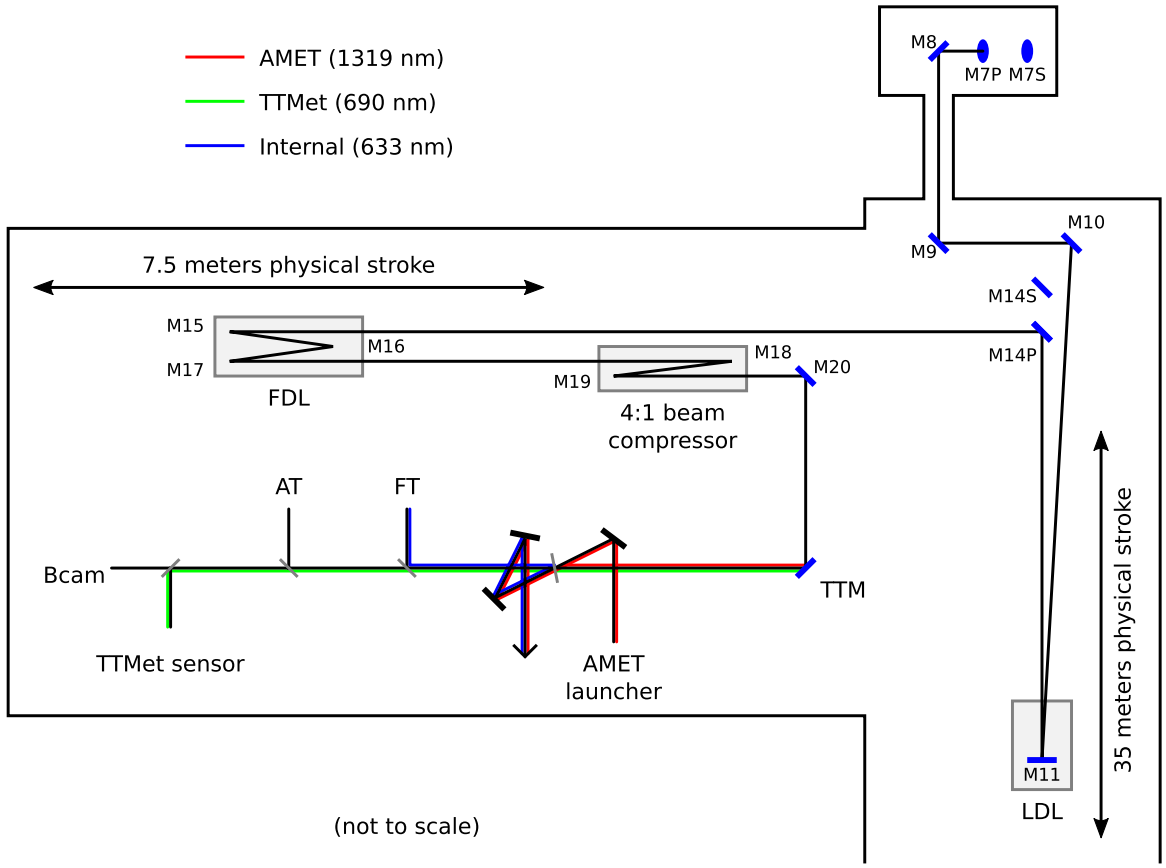

Figure 3. Optical layout in the interferometric basement, showing the Keck II primary beam path only. M7P is located under the telescope, aligned with its azimuth axis; M7S is the equivalent mirror for the secondary beam train, but off the azimuth axis and therefore tracking. From M8 to M11, these rectangular beam train mirrors accommodate primary and secondary beams. M11 is a steering flat mirror mounted on the long delay-line cart (LDL). Starting with M14P and M14S, the primary and secondary beams are sent to separated fast delay lines (FDLs, M15 to M17). The beams are then compressed (M18–M19) by a factor of four from 124 mm to 31 mm. M20 finally folds the beam toward the beam combining lab. Measurements from the angle tracker (AT) are used to control the tip-tilt mirrors (TTMs) to stabilize the injection into the fringe tracker (FT). Specific to ASTRA, the tip/tilt metrology (TTMet) works in parallel with the angle tracker to control the tip/tilt mirrors, providing a reasonable control bandwidth on internal tip/tilt errors, when observing faint objects. The metrology light in the beam combining area is color-coded with the following: AMET 1319 nm metrology in red, TTMet 690 nm metrology in green, and internal 633 nm FT metrology in blue. Not color-coded, the stellar *K* band goes to the fringe tracker (FT) and the stellar *H* band goes to the angle tracker (AT).

(A color version of this figure is available in the online journal.)

strive to limit the correction from the phase-referencing fringe tracker to the atmospheric differential piston, contributing to the instrument sensitivity, but also compensate for differential OPD between the primary and secondary beams, making phase-referencing possible. Figure 4 summarizes the various aspects of the internal OPD control. Accelerometers are detailed in Section 2.2.1, astrometric and internal metrologies in Section 2.2.2, and AO tip/tilt-induced piston compensation in Section 2.2.3.

2.2.1. Accelerometers

The same accelerometers used by other Keck Interferometer instruments participate in the reduction of piston vibrations introduced by the telescopes. However, since the longitudinal metrology (detailed in following Section 2.2.2) reaches further inside the AO system compared to previous Keck Interferometer instruments (e.g., Keck Nuller; Colavita et al. 2009), the accelerometers measuring the relative vibrations between the AO bench and the DSM are turned off, while keeping the telescope primary mirror, tertiary mirror, and AO bench accelerometers on. Even though the secondary mirror is also equipped with accelerometers, their contribution has always been turned off due to the fact that the focus offload from the AO system to the secondary mirror exceeds the accelerometer dynamic range and causes transient saturation of the accelerometer compensation. Some of the vibration residuals seen by the fast fringe tracker (see Section 3.1) are certainly predominantly coming from the telescope secondary mirrors. The combined accelerometer measurements at each telescope are then sent for compensation to the appropriate fast delay lines (FDL, see Figure 4).

2.2.2. Longitudinal Metrology

The main component of the internal optical path length control is an infrared 1319 nm laser (JDSU NPRO-125N-1319) heterodyne metrology system, named AMET for Astrometric METtrology.[11] It is similar in concept to the Common-Path Heterodyne Interferometer gauge developed for the Space Interferometry Mission (Zhao et al. 2003) where orthogonal masks are used to isolate two metrology propagations, with a low level of self-interference and cross-talk. In the ASTRA implementation, an annular mask, letting the central star light through, selects the propagation through the beam train up to a corner cube located at a pupil location just in front of the AO system's DM. A central mask selects the annular propagation

[11] Reflecting the narrow-angle astrometry application.

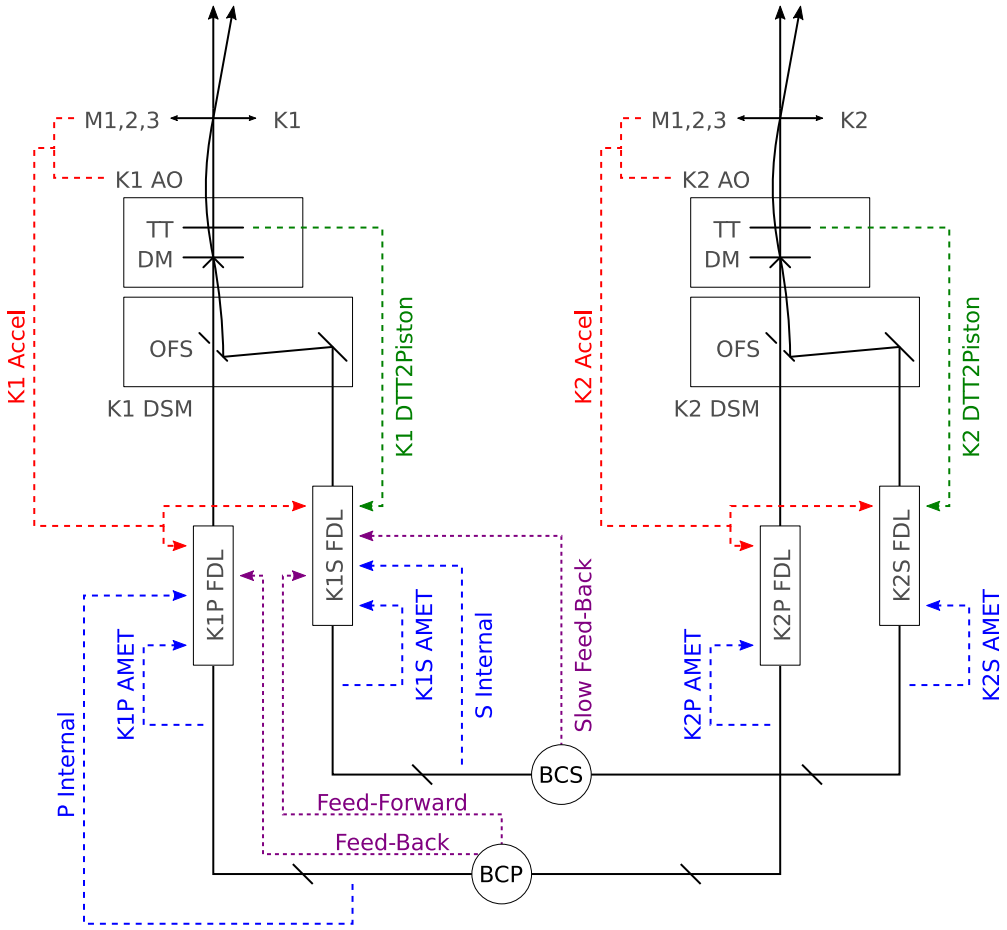

Figure 4. Overview of the internal optical path control, including accelerometers (Accel), AO tip/tilt-induced differential piston compensation (DTT2Piston), and longitudinal metrology (AMET and Internal). All three measurements are fed-forward to the fast delay lines (FDL) to stabilize the OPD. The primary beam combiner (BCP) measures the fringe position and sends fast feed-back/feed-forward to the primary/secondary FDLs, respectively. The fringes are stabilized for the secondary beam combiner (BCS), that only needs to correct for slow drifts with a feed-back to the secondary FDL.

(A color version of this figure is available in the online journal.)

to a reference corner cube located on the opposite side of the AMET injection beam splitter. Each of the four metrologies, one per beam train, measures the difference between the injection dichroic to DM corner cube and the injection dichroic to reference corner cube optical paths. To complete the beam train coverage, another existing metrology system (named Internal, and re-purposed from the Nuller instrument) based on a single stabilized HeNe laser source, measures the on-axis OPD from the beam combiner beam splitters to the AMET reference corner cubes. The propagation selection for this visible system is based on orthogonal polarizations selected with linear polarizers. For the reference corner cube to work with both systems, it is composed of an on-axis inner mask that blocks the infrared system, and also selects a single linear polarization for the visible system. Figure 5 gives a summary of the AMET and Internal setup.

The detection electronics for the infrared system is an exact replica of the 633 nm metrology systems except for the detector cards modified to operate at 1319 nm (more details on the detection chain can be found in Colavita et al. 2013). It is capable of measuring optical path evolution with an accuracy of 2.5 nm to frequencies up to 4 kHz.

The single infrared laser source of the AMET does not have a stabilized wavelength. Instead, it is operated at a differential OPD close to zero in order to cancel any impact of the wavelength fluctuation on the differential OPD control. This can be achieved, in our setup, by adjusting the position of the reference corner cubes to match the differential OPD in the delay lines. In practice, this is equivalent to a transfer of the differential OPD measurement to the visible HeNe metrology system, which already meets the wavelength stability requirement without the need for additional stabilization of the 1319 nm source.

However, the wavelength fluctuations can cause a degradation of the OPD control of a single beam train. On the fast fringe tracker timescale of typically 1 ms, the amplitude of the effect is estimated to be a negligible 2 nm for a maximum OPD of 85 m (laser line width smaller than 5 kHz ms^{-1}) and does not cause significant contrast losses. On second timescales, this wavelength fluctuation appears as an additional turbulence-like term of 37 nm$_{\rm RMS}$ over the same 85 m delay (estimated from a laser frequency drift smaller than 50 MHz hr^{-1}), correlated between primary and secondary targets, and therefore perfectly well corrected by the bright primary fringe tracker.

Both visible and infrared systems are relative metrology systems: they only provide an accurate optical path variation relative to an offset, which can be assumed to be fixed as long as the metrology systems stay uninterrupted. The determination of this offset, only needed for astrometry, would have been achieved through a swap of the observed pair of targets between the primary and secondary beams. This operation corresponds

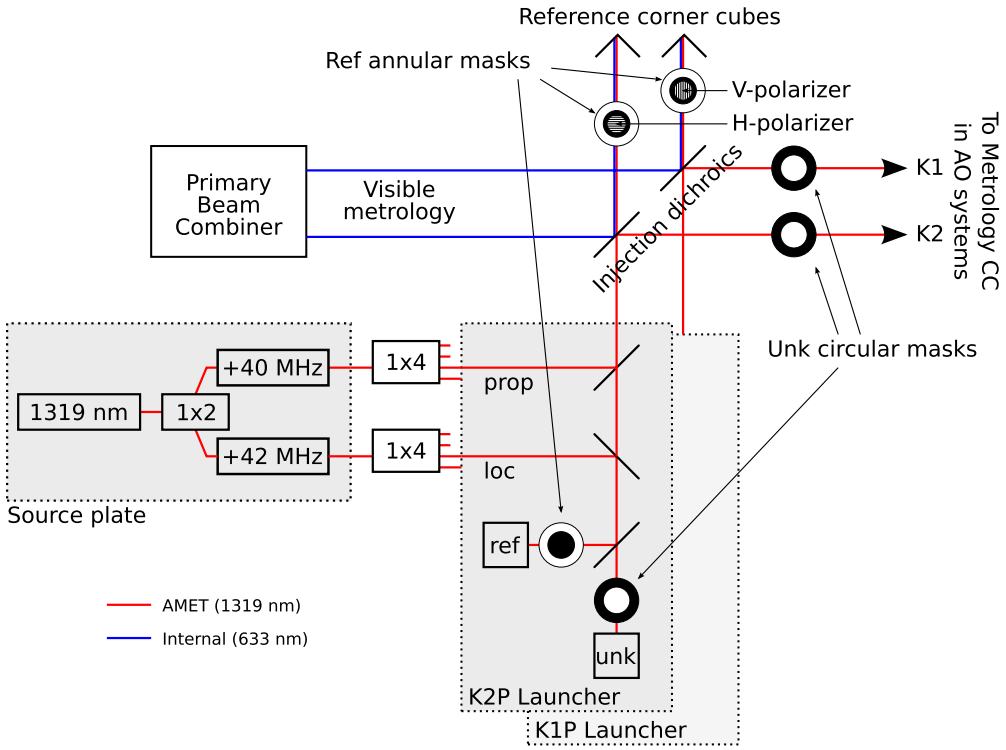

Figure 5. Schematic of the longitudinal metrology, with only the primary beam trains shown. The infrared 1319 nm (red) metrology reference output (Ref) measures the optical path from the launcher to the reference corner cube, and the unknown output (Unk) measures from the launcher to the metrology retro-reflector (not shown) inside the AO systems. The visible 633 nm metrology (blue) measures in differential from the beam splitter inside the beam combiner to the reference corner cubes. All three combined, the longitudinal metrologies measure the optical path difference from the beam combiner beam splitter to the common metrology corner cubes in the AO systems, providing a metrology coverage matching the starlight path, from K1 and K2 telescopes to beam combiner. The masks are responsible for selecting which beam path is measured by which system: non-overlapping circular and annular masks separate the infrared Ref and Unk of a given beam train, whereas for the visible system, H-polarizers and V-polarizers separate the K1 beam from the K2 beam.

(A color version of this figure is available in the online journal.)

to a sign change for the separation vector, which causes the half sum of the differential OPD to give the metrology offset directly.

Finally, since each FDL has a local metrology system, the difference between longitudinal metrology and delay line local metrology can be sent for compensation in feed-forward (unit gain) to the FDL servomechanism (servo, see Figure 4).

2.2.3. AO Tip/Tilt-induced Piston Compensation

The tip/tilt mirror of the Keck AO system is not in a pupil plane. Consequently, the positions of the primary and secondary beams are not the same on this mirror, and the mirror motion therefore introduces a variable differential OPD.[12] Based on the geometry of the tip/tilt mirror inside the AO system, illustrated in Figure 6, the amplitude of the uncorrected effect has been estimated to a significant 528 nm arcsec^{-2} of induced pistons per arcsecond of corrected tip/tilt and arcsecond of separation (see Appendix A.1 for calculation details). For a good Mauna Kea seeing of 0.5 arcsec, and a typical separation of 15 arcsec, this amounts to a differential OPD of 0.89 μm$_{\rm RMS}$, or a drastic 96% fringe contrast reduction per telescope on long exposures at 2.2 μm. Consequently, using the same infrastructure as the

[12] Following Woillez & Lacour (2013), this differential OPD can be re-interpreted as a modulation by the AO tip/tilt mirror of the metrology corner cube conjugate in primary space, affecting the astrometric or co-phasing baseline on the order of $\delta B_{\rm Dtt} = \pm 12$ cm. The amplitude of this baseline modulation was verified directly with the Internal Baseline Monitor Transverse designed for narrow-angle astrometry: a camera installed inside the AO system responsible for measuring the conjugation of the metrology corner cube in primary space.

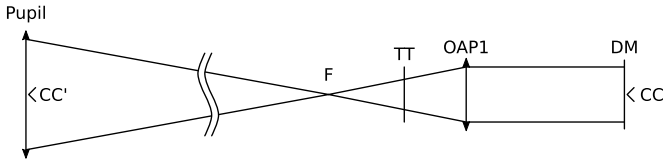

Figure 6. Geometry of the tip/tilt mirror (TT) inside the AO system. The longitudinal metrology corner cube retro-reflector (CC) is located in front of the AO deformable mirror (DM), conjugated (CC′) with the telescope pupil. The tip/tilt mirror (TT) is located between the telescope focus (F) and the first collimating off-axis parabola (OAP1). Not located in a pupil plane, it induces a differential piston between primary and secondary beams. An estimation of the effect based on this geometry is given in Appendix A.1.

accelerometers, the motion of the tip/tilt mirror is digitized and sent to the FDL controllers, where it is projected on the separation between secondary and primary targets. The result is used as an additional target contribution to the FDL servo, as shown in Figure 4.

2.3. Phase-referencing Architecture

Once the instrumental piston and tip/tilt are adequately corrected, the phase-referencing performance relies on the fast on-axis fringe tracker to stabilize the fringes and send the proper correction to the faint off-axis instrument where long integrations are performed.

2.3.1. Fringe Trackers

The principle and performance of the Keck Interferometer fringe trackers have been extensively documented in Colavita

et al. (2010). The fringe trackers are routinely used to perform V^2 measurements, as well as to stabilize the OPD for the Nuller instrument. Specific to ASTRA, and already detailed for the SPR instrument (Woillez et al. 2012), two distinct cameras, associated with the primary and secondary beam combiners BC-P and BC-S in Figure 4, are available to operate the two fringe trackers at different rates: 250 Hz for the phase-referencing fringe tracker and down to a fraction of Hz for the phase-referenced fringe tracker.

The fringe trackers' flux and fringe acquisition procedures have been adapted to the DFPR, mainly to deal with the intrinsically faint object on the faint phase-referenced fringe tracker: running at a very slow rate, it cannot be used to search for fringes over long OPD ranges. First, the flux is optimized and the fringes are found for the phase-referencing fringe tracker with the bright target. Then with a telescope offset, the bright target is sent to the phase-referenced fringe tracker, temporarily running at a fast rate, to quickly perform the same acquisition operations. Finally, with the bright target back on the phase-referencing fringe tracker, and the faint target on the phase-referenced fringe tracker, the actual phase-referenced observations can start, with the phase-referenced fringe tracker already a few coherence envelopes away from the faint object fringes. These operations are supervised by the interferometer sequencer already mentioned in Section 2.1.2.

2.3.2. Feed-back, Feed-forward

The fast primary fringe tracker operates in a feed-back loop of gain lower than unity with its own primary delay lines. Typically running at a 250 Hz fringe rate, the primary fringe tracker provides a control bandwidth with a 0 dB crossover on the order of 16 Hz. Since each fringe tracker has its own delay lines, as illustrated in Figure 4, the fast primary fringe tracker is able to send an open-loop correction (gain of 1) to the secondary delay lines, providing an OPD correction better than the closed-loop correction to the primary side in the 0–60 Hz range. This feed-back/feed-forward architecture principle for the DFPR instrument is similar to the one used for the NULLER (Colavita et al. 2009) and SPR (Woillez et al. 2012) instruments. The only major addition is the capability to exchange which of the two fringe trackers is phase-referencing the other based on the magnitudes of the observed pair, which is controlled by the interferometer sequencer[13].

The two fringe trackers are also connected through their state machines. The slow fringe tracker loop is systematically put on hold when the primary fringe tracker is not properly tracking: locked on and within 1 μm of the central fringe. This hold mechanism is also used to select which fringe measurements from the slow off-axis fringe tracker are kept by the data reduction pipeline. This hold mechanism is again completely identical to the one in place for the SPR instrument (Woillez et al. 2012).

3. PERFORMANCE

To characterize the on-sky performance of the DFPR, we have considered three aspects. First, as detailed in Section 3.1, we present the performance of a single bright fringe tracker, which sets the limiting magnitude for the reference target. Then, as detailed in Section 3.2, we look into the correlations in OPD measurements between bright pairs. This information is used to predict the fringe contrast and maximum integration time for the phase-referenced target, therefore defining the sensitivity of the instrument. Last, detailed in Section 3.3, we describe actual contrast measurements performed with the slow fringe tracker on the faint object of a bright–faint pair and verify the predicted performance.

3.1. Bright Fringe Tracker Performance

3.1.1. Active Compensation

Despite a passive mitigation campaign carried out throughout the observatory, a level of piston vibration compatible with efficient fringe tracking could only be achieved with the help of active systems: a combination of telescope accelerometers and longitudinal metrology, described in Sections 2.2.1 and 2.2.2, respectively. The AO tip/tilt-induced piston compensation provides a correction well within the fringe tracker control bandwidth and therefore does not have any significant impact on the fringe tracking performance. The optical path fluctuations measured by these systems are presented in Figure 7. At 10 Hz, which is the -3 dB corner of the fringe tracker error rejection (see Colavita et al. 2010), the total measured vibrations are on the order of 0.4 μm^2, which would correspond to a fringe contrast reduction to 4%.

3.1.2. Fringe Tracking Performance

The remainder of the instrumental fluctuations and the atmospheric piston are compensated by the fast fringe tracker, with typical values presented in Figure 8. The active compensation systems correct for $\sim$1.36 μm_{RMS}, mostly vibrations (1–100 Hz), whereas the fringe tracker compensates for $\sim$11.1 μm_{RMS} of low frequency vibrations (1–10 Hz) and turbulent pistons ($\lesssim$10 Hz). The fringe tracking residuals at this $K = 7.45$ mag are observed at $\sim$242 nm_{RMS}. The use of a longitudinal metrology reaching further inside the AO system and co-aligned with the stellar beam enabled us to obtain better fringe tracking residuals than in Colavita et al. (2010), as shown by a typical phase jitter below 0.5 rad_{RMS}.

Figure 8 also gives an indication of the fast fringe tracker performance versus frequency. For the feed-back, the phase fluctuations are attenuated below 16 Hz and slightly amplified above this cutoff. The feed-forward advantage around the cutoff frequency is obvious: at 7 Hz, the feed-forward residuals are $\sim$120 nm_{RMS}, better than the $\sim$210 nm_{RMS} feed-back residuals. The additional feed-forward amplification above the cutoff completes a feed-back versus feed-forward picture, as described in Lane & Colavita (2003) and Colavita et al. (2010).

3.1.3. Limiting Magnitude

The limiting magnitude of the bright fringe tracker is driven by the quality of the correction it must provide to the slow off-axis secondary instrument. In the current ASTRA configuration, where the off-axis instrument is an identical *K*-band fringe tracker with which an absolute V^2 measurement is intended, the primary fringe tracker rate is set to 1250 Hz (fringe rate of 250 Hz) in order to achieve a high off-axis fringe contrast. As shown in Figure 8, the off-axis residuals are $\sim$117 nm_{RMS} at 10 Hz, providing a square fringe contrast of 0.89. If the off-axis instrument were operating at longer wavelengths, using the *L*-band fringe tracker (Ragland et al. 2009) or the *N*-band Keck Nuller (Colavita et al. 2009) for V^2 measurements, or if the off-axis *K*-band fringe tracker measured differential phases

[13] This functionality is necessary for the astrometric swaps and is also useful for the flux and fringe acquisition described in Section 2.3.1.

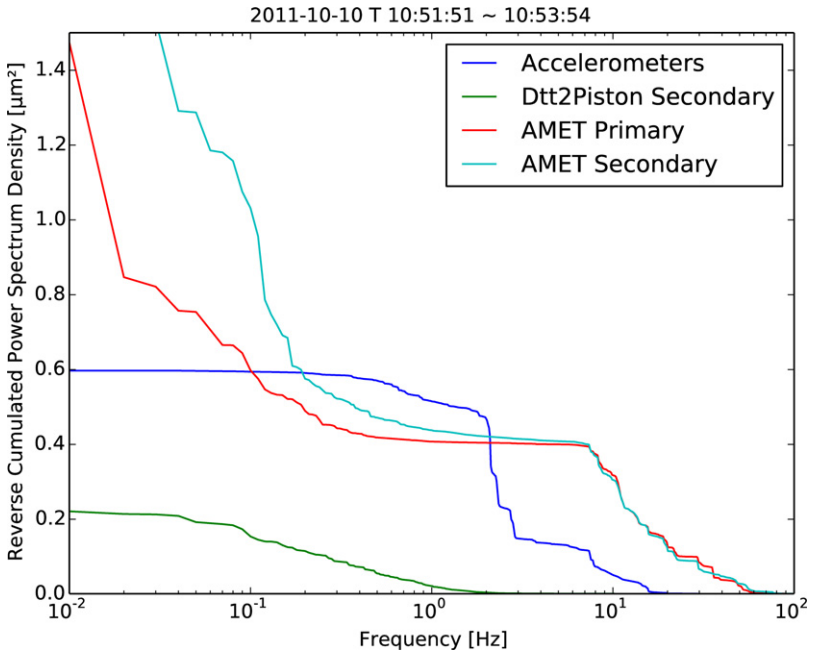

Figure 7. Optical path fluctuations measured by the active optical path compensation systems, in DFPR configuration: accelerometers common to primary and secondary beams, AO tip/tilt-induced piston compensation (Dtt2Piston) for secondary beam only, and longitudinal metrology (AMET) for primary and secondary beams. The quantity represented is the reverse cumulated power spectrum density of a typical optical path fluctuation measurement carried out over an interval of 10 s. The normalization is such that when the frequency approaches zero, the limit is the optical path fluctuation variance. As such, each jump represents the contribution of a vibration, with the amplitude of the jump directly related to the contribution to the variance.

(A color version of this figure is available in the online journal.)

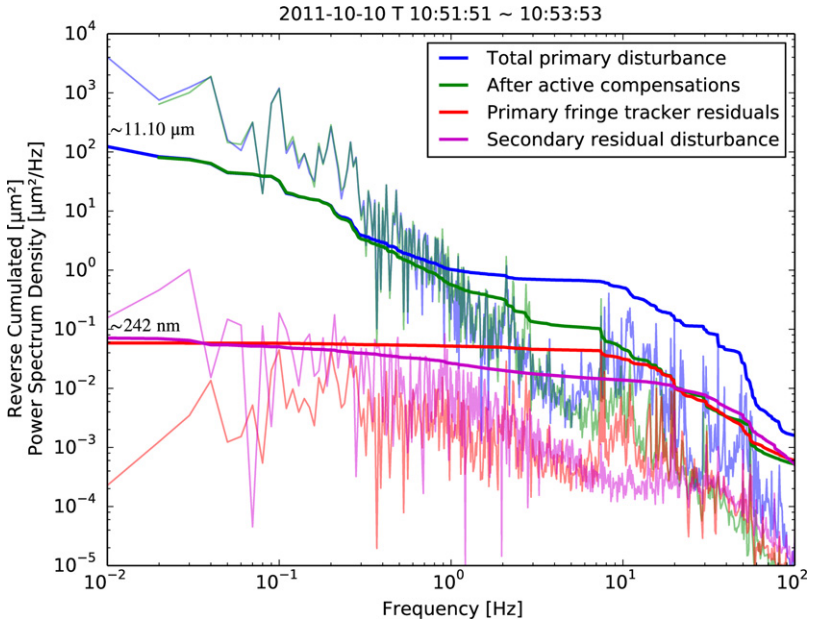

Figure 8. Typical OPD control performance provided by the fast primary fringe tracker, obtained on a bright $K = 7.45$ target. Both the power spectrum densities (thin lines) and the reverse cumulated power spectrum densities (thick lines) are given for each of the total primary OPD disturbance of atmospheric and instrumental origins (blue), the OPD disturbance after active compensations correction by metrology and accelerometers (green), and the fast primary fringe tracker residuals (red). The secondary residual disturbance (magenta) represents the OPD fluctuations measured by a passive off-axis fringe tracker, after feed-forward correction from the primary. The two values given along the y-axis of the figure correspond to the square root of the reversed cumulated power spectrum density at 10^{-2} Hz: 11.10 μm_{RMS} for the total primary disturbance and 242 nm_{RMS} for the primary fringe tracker residuals.

(A color version of this figure is available in the online journal.)

and visibilities with an off-axis adaptation of the SPR instrument (Woillez et al. 2010), this off-axis contrast requirement could probably be reduced and the primary fringe tracker rate decreased to improve the limiting magnitude.

If the limiting magnitude estimation follows the same procedure as in Colavita et al. (2013, see Tables 2 and 3), a signal-to-noise ratio (S/N) of ~10 is required on the phase estimation, adding a 2× margin (0.7 mag) to deal with non-ideal atmospheric conditions. Adapting the standard V^2 limiting magnitude of $K = 10.3$ at a 100 Hz fringe rate to 250 Hz (frame rate of 1250 Hz), the estimated limiting magnitude would become $K = 9.3$. In practice, this limit was never reached, being closer

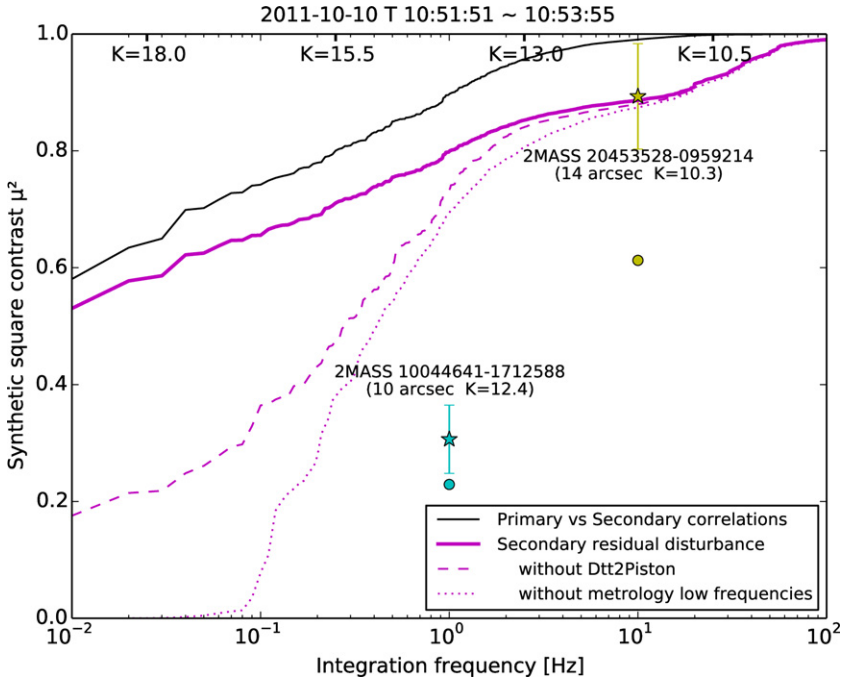

Figure 9. Synthetic square contrast loss μ^2 vs. integration frequency, estimated for the same 7.4 arcsec separation bright-bright ($K = 7.45/K = 7.87$) pair (Two Micron All Sky Survey (2MASS): 01174326−1220413/01174320−1220339) as in Figure 8. The first estimation, primary vs. secondary correlations (thin black), is based on the fringe phase correlations measured on the two beams, a combination of the longitudinal metrology, the AO tip/tilt-induced piston compensation, the fringe trackers residual phases, and the sidereal differential optical path difference. The second estimation, secondary residual disturbance (thick magenta), corresponds to how much phase motion is actually measured by the secondary fringe tracker, when feed-forward from the primary fringe tracker is applied. The following two estimations show the square contrast losses associated to the AO tip/tilt-induced piston (without Dtt2Piston, magenta dashed), and to the 2 s high-pass metrology filter (without metrology low frequencies, magenta dotted). Also, based on the fast fringe tracker limiting magnitude of $K = 8$ at 250 Hz, an indication of the K band sensitivity is given in the top of the figure, with the assumption that it scales with the integration frequency. The two datapoints, 2MASS 10044641−1712588 and 2MASS 20453528−0959214 are actual off-axis contrast measurements, with indication of the pair separation and the faint target K band magnitude. The circles corresponds to raw contrasts, whereas the stars are corrected from the fast fringe tracker jitter evolution, a measurement of the atmospheric conditions. For 2MASS 10044641−1712588, the disagreement with respect to the prediction is probably related to the poor atmospheric conditions (strong high altitude seeing and high wind per the Mauna Kea Weather Center).

(A color version of this figure is available in the online journal.)

to $K = 8$. This contrasts with the fact that simulating an S/N of 10 leaves Figure 8, which was obtained at an S/N of ∼1000, virtually unchanged. This discrepancy can be explained by the fluctuations of the injection into the fringe tracker: they require a higher mean flux level to limit the occurrence of unwrapping errors caused by transient low injection states. For the Nuller (Colavita et al. 2009), the impact of scintillation was addressed by installing irises at the fringe tracker inputs, which stabilized the injection at the expense of a brighter limiting magnitude. Contrary to the Nuller and its brighter targets ($K < 3.7$ in Millan-Gabet et al. 2011), scintillation has a direct impact on the sky coverage of off-axis fringe tracking.

3.2. Fringe-tracking on Bright Pairs

By observing bright pairs, we are able to measure the amount of decorrelation between the primary and secondary fringe trackers that is introduced by the instrument and the atmosphere. This quantity can then be used to assess how well off-axis fringe-tracking would perform when the faint fringe tracker is slowed for long integrations. The square contrast loss factor μ^2, for a given integration time T can be related to the power spectrum density of the phase fluctuations one-sided PSD(ν), using

$$\mu^2(T) = e^{-\int_{1/T}^{+\infty} \mathrm{PSD}(\nu)\, d\nu}. \quad (1)$$

This is the quantity used to construct Figure 9.

3.2.1. Primary and Secondary Correlations

First, we looked into the correlations between the two fringe trackers. We computed the following astrometric-like error,

$$\epsilon = \underbrace{(\Delta\mathrm{Met} + \Delta\Phi)}_{\text{internal}} - \underbrace{(\delta \boldsymbol{B}_{\mathrm{Dtt}} \cdot \Delta\boldsymbol{s} + \boldsymbol{B} \cdot \Delta\boldsymbol{s})}_{\text{external}}. \quad (2)$$

On one side, it includes the internal contributions, total differential metrology signal ΔMet and differential residual phase of the two fringe trackers ΔΦ, and on the other side, the external contributions, AO tip/tilt-induced piston compensation $\delta\boldsymbol{B}_{\mathrm{Dtt}}$ re-interpreted as a baseline error and sidereal term $\boldsymbol{B} \cdot \Delta\boldsymbol{s}$. In the absence of an isoplanatic atmospheric piston, this error ϵ should be zero; a departure leads to a contrast loss factor on the slow phase-referenced side depending on the integration frequency $1/T$ as stated in Equation (1). A typical result is shown in Figure 9, "primary vs. secondary correlations," for a small separation case, where the atmospheric contribution is negligible, therefore illustrating the instrumental errors. For integration frequencies higher than 1 Hz, the level of correlation is quasi-perfect and corresponds to a predicted square contrast loss factor above 0.95. This shows that no fundamental instrumental error affects the behavior of the system at these frequencies. The degradations that occur at time scales T larger than 10 s have not been thoroughly investigated: this is the realm of very faint sources beyond the reach of the instrument where getting the faint object light into the fibers of the off-axis instrument

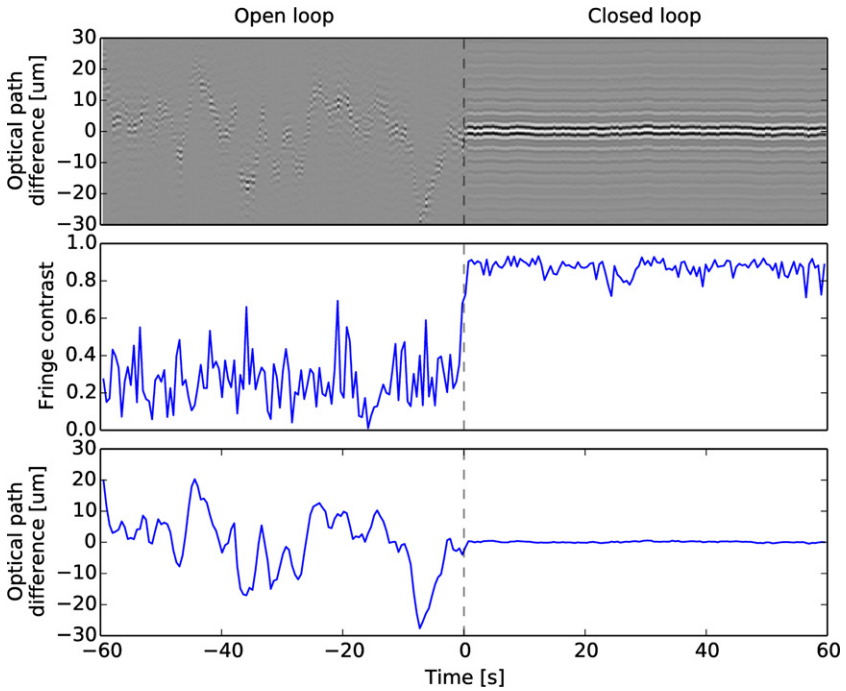

Figure 10. Top: synthetic off-axis *K*-band fringe packet intensity (gray scale) reconstructed over an optical path difference range of $-30\,\mu$m to $+30\,\mu$m (vertical axis) for an integration period of 0.5 s, displayed vs. time (horizontal axis). At time zero, the previously open fringe tracking loop is closed: the fringe position is stabilized and the contrast increases. This illustrative simulation is based on the same data set used in Figure 9. Middle: corresponding instantaneous fringe contrast. Bottom: corresponding instantaneous fringe phase.

(A color version of this figure is available in the online journal.)

becomes harder than detecting faint fringes themselves. The origin of this decorrelation can only be guessed. Based on the similitude with the impact of the AO tip/tilt-induced piston, also shown in Figure 9, its partial correction seems like the most probable culprit. Note that these decorrelations would have had a drastic impact on an eventual astrometric application.

3.2.2. Secondary Residuals

We then looked at the residuals measured by the off-axis fringe tracker when receiving the feed-forward correction. This configuration gives a more accurate estimation of what to expect when this fringe tracker is slowed down on fainter objects. As shown in Figure 9, the main difference is a drop in square contrast to 0.9 around the 16 Hz fast fringe tracker control bandwidth. This corresponds to the previously mentioned $\sim$117 $\mathrm{nm_{RMS}}$ at 10 Hz of secondary residual disturbance shown in Figure 8.

The ASTRA longitudinal metrology follows the same control pattern as the cloudé metrology, presented in Colavita et al. (2013), where the piston measurements are high-pass filtered before correction by the FDLs. This implementation makes the system more tolerant to metrology breaks, but the internal OPD fluctuations on time scales longer than the filter time constant of $\tau = 2$ s are not corrected. This effect is responsible for the coherence losses at sub-hertz integration frequencies in Figure 9, "without metrology low frequencies." However, this is the configuration used for the fringe contrast measurements with integration frequencies in the 1–10 Hz presented in the following section. Ideally, but considered too late, this filter time constant should have been increased as soon as the integration frequency fell below 10 Hz.

Finally, Figure 10, based on the same data set as Figure 9, provides a direct illustration of the benefits and performance of off-axis fringe tracking: closing the fringe tracking loop improves the fringe contrast of long integrations and stabilizes the fringe position. This illustration is an optical interferometry equivalent of the open-loop versus closed-loop illustrations shown with AO (Rousset et al. 1990).

3.2.3. Atmospheric Contribution

The contribution of the atmosphere to the differential piston has been studied by Daigne & Lestrade (2003) for the range of integration frequencies (10^2 Hz to 10^{-2} Hz) in which we are interested. Although focused on the Very Large Telescope Interferometer on the Unit Telescopes, their models are for an observing configuration and atmospheric conditions (0.65 arcsec seeing) similar to what we had for our bright pair study (0.55 arcsec seeing per the Mauna Kea Weather Center seeing monitor[14]). We therefore used their estimations as an order of magnitude assessment.

For the separation of 7.4 arcsec considered in Figure 9, the atmospheric contribution μ^2_{atm} is negligible compared to the instrument contribution even for the lowest exposure frequencies ($\mu^2_{\mathrm{atm}} = 0.8$–$0.9$ down to 10^{-2} Hz). The atmospheric contribution would only become comparable to the instrument contribution for separations on the order of 20 arcsec and only for integration frequencies beyond 1 Hz. In practice, and as illustrated in the following section, the instrument was never pushed beyond this 20 arcsec separation and 1 Hz integration frequency limit.

3.3. First Faint Contrast Measurements

Ultimately, the goal of off-axis fringe tracking was to observe intrinsically fainter objects, measuring visibilities similar to,

[14] http://mkwc.ifa.hawaii.edu/current/seeing/

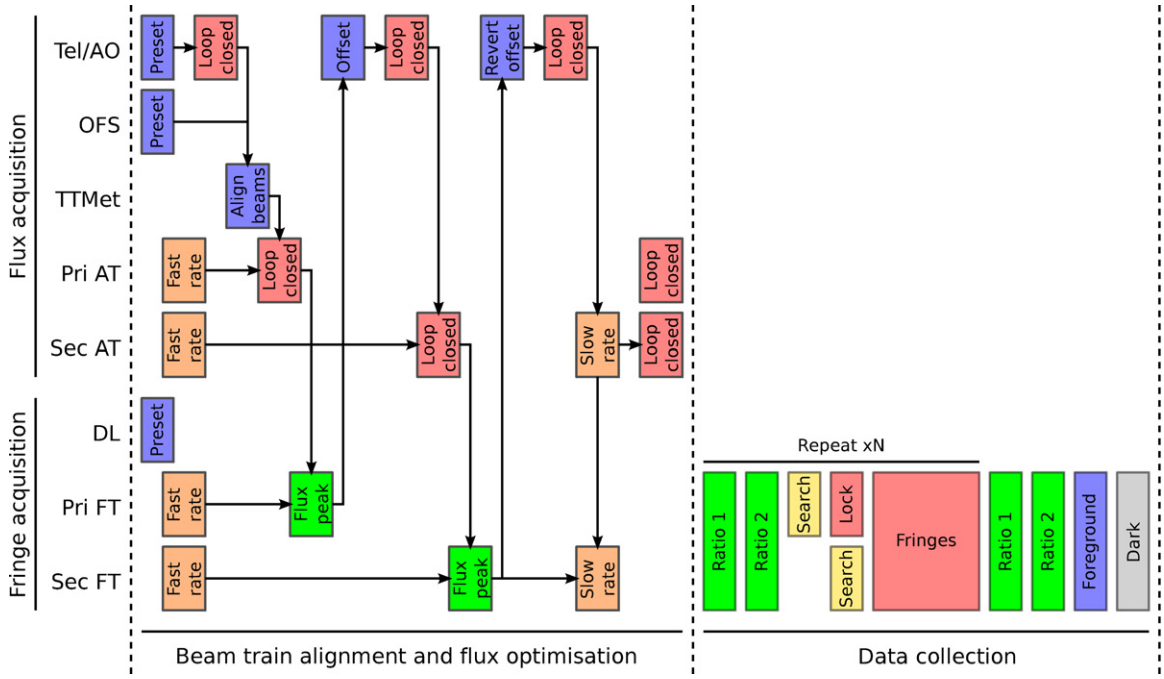

Figure 11. Off-axis observing sequence is an evolution of the standard V^2 observing sequence (e.g., Woillez et al. 2010, Figure 4). The beam trains' alignment and flux optimization into the fringe trackers are adapted to the faint target. Following a preset of the telescopes (Tel), adaptive optics (AO), and delay lines (DL), the tip/tilt metrology (TTMet) is used to align the beam trains and off-axis field selectors (OFS) to the separation of the pair. Then, the bright target is used to optimize in sequence the injection into the primary and secondary fringe trackers (Pri/Sec FT), sending offsets to the respective angle trackers (Pri/Sec AT). Finally, after configuration of the frame rates of the FT and AT a standard V^2 is carried out in parallel on the primary and secondary targets.

(A color version of this figure is available in the online journal.)

e.g., the V^2 instrument (Colavita et al. 2010) or differential visibilities and differential phases similar to, e.g., the SPR instrument (Woillez et al. 2012).

The first off-axis faint fringe detection was performed on UT 2012 January 22, on a $K = 11.5$ target, with a $K = 7.0$ reference 10 arcsec away. As the instrument performance progressed, the sensitivity reached $K = 12.4$ on UT 2012 May 20, with the same kind of reference target. Then, on UT 2012 February 9T12:20, 6 months before the closure of the Keck Interferometer (Wizinowich 2011), the DFPR instrument started carrying out actual contrast measurements, following the same calibration procedure as for the V^2 instrument (dark and flux ratio measurements detailed in Colavita et al. 2010). With an emphasis on the specifics of off-axis fringe tracking, namely the optimization of the flux injected into the fringe trackers using only the bright reference and the simultaneous calibrated fringe collection on the fast bright primary and slow faint secondary, the observing sequence is illustrated in Figure 11.

Figure 9 presents two such contrast measurements. In order to compare them to the secondary fringe tracker residuals measured on bright pairs, they were corrected from the evolution of the phase jitter of the fast fringe tracker between the different measurements, presumably related to the different turbulent conditions. In the case of *2MASS 20453528−0959214* the primary fringe tracker phase jitter was measured at 215 nm instead of the 120 nm mentioned in 3.2.2. The resulting corrections by a factor of 1.30 to $\mu^2 = 0.89 \pm 0.09$ show a good agreement with the predicted synthetic square contrast. The pertinence of this correction highlights the sensitivity of the off-axis contrast measurement to the fast fringe tracker performance, extending to off-axis the on-axis case presented by Mérand et al. (2010) using AMBER and FINITO data on the VLTI.

2MASS 10044641−1712588. First faint contrast measurement (circle), with the DFPR off-axis fringe tracking instrument slowed down to an integration frequency of 1 Hz, obtained on a $K = 12.4$ target, with a $K = 7.9$ reference (TYC 6050-1110-1) 10 arcsec away. The observed contrast is significantly lower than the estimations presented, which is certainly a consequence of poor seeing: there was no MASS/DIMM measurement available from the Mauna Kea Weather Center due to wind speeds higher than 50 km hr^{-1}, but the high altitude seeing estimate from the Weather Research and Forecasting Model was 1.2 arcsec, peaking at 1.8 arcsec at the beginning of the night). This observation acts as a reminder that off-axis fringe tracking is sensitive to atmospheric conditions.

2MASS 20453528−0959214. Last faint contrast measurement (circle), corrected to $\mu^2 = 0.84 \pm 0.09$ from the 120 nm to 215 nm differential jitter (star); this time matches the prediction. This measurement was obtained at 10 Hz on this $K = 10.3$ target, with a $K = 8.8$ reference (TYC 5760-1999-1) 14 arcsec away. The measured seeing was around 0.55 arcsec.

The correction above addresses only the residual contribution of the on-axis turbulence, not the anisoplanatic contribution. This may provide an explanation for the lower than expected contrast measured on *2MASS 10044641−1712588*, performed under a stronger high altitude turbulence than in the case of *2MASS 20453528−0959214*.

4. CONCLUSION

Between 2011 January and 2012 July, the DPFR instrument was used to demonstrate the first faint dual-field off-axis observations in Optical Long Baseline Interferometry. Unfortunately, this demonstrator was never given the time needed to become an

operational facility with a guaranteed performance. This would have required a characterization of the performance dependence on the atmospheric turbulence conditions, providing a simultaneous test of the turbulence models in the piston perspective. In addition, the demonstration of the calibration of the contrast measurement into visibilities would have been performed at least by cross-calibrating unresolved calibrators and at best by comparing calibrated visibilities to expectations from known objects.

Nevertheless, this first demonstration provides valuable insights into the challenges of off-axis fringe tracking for current and future interferometric projects. Somewhat overlooked by force of habit, the tip/tilt acquisition of the faint object turned out to be a limiting factor of the off-axis sensitivity, stronger than the optical path control. In retrospect, a completely blind relative and accurate off-axis tip/tilt acquisition capability should have been a top priority since the project's inception.

The sky coverage of off-axis fringe tracking depends heavily on the limiting magnitude of the interferometer. As such, the sensitivity improvements provided by off-axis fringe tracking should not overshadow any work that would improve the on-axis limiting magnitude, which is known to be impacted by low beam train transmission. In addition, unless the limiting magnitude on smaller telescope arrays is greatly improved, off-axis fringe tracking is really something for an interferometer in the KI or VLTI-UT class.

Finally, despite the limited time of KI operations available for use with the DFPR instrument, we did observe one AGN. We will present the results of this observation, addressing some of the visibility calibration concerns, in an upcoming paper.

The ASTRA project was supported by the National Science Foundation Major Research Instrumentation grant AST-0619965. The Keck Interferometer was funded by the National Aeronautics and Space Administration as part of its Exoplanet Exploration program. The authors wish to recognize and acknowledge the very significant cultural role and reverence that the summit of Mauna Kea has always had within the indigenous Hawaiian community. We are most fortunate to have the opportunity to conduct observations from this mountain.

APPENDIX

A.1. Keck AO Tip/Tilt-induced Piston

The Keck AO tip/tilt mirror is not in a pupil plane and therefore introduces a differential piston between the on-axis primary and the off-axis secondary as it corrects the turbulent tip/tilt. Since the path through this mirror is not measured by any metrology system, the differential piston effect must be estimated from the actual position of the mirror. The geometry considered here is that of an on-axis beam falling at the center of the tip/tilt mirror, and an off-axis secondary beam falling off-center with the motion of the tip/tilt mirror generating the piston. The amplitude of this piston is directly proportional to the separation, and to the amplitude of the tip/tilt corrected by the mirror. The bandwidth of the introduced piston is directly related to the bandwidth of the AO tip/tilt correction (under 100 Hz for a control loop running at 1 kHz).

Based on the geometry and parameters shown in Figure 6 and Table 1, respectively, the physical tilt $\theta_{\rm TT}$ of the AO tip/tilt mirror, correcting an incoming atmospheric tilt $\theta_{\rm Tilt}$, can be written as

$$\theta_{\rm TT} = \frac{F_{\rm tel}\ \theta_{\rm Tilt}}{2\ L_{F-{\rm TT}}}, \tag{A1}$$

where $F_{\rm tel}$ is the effective telescope focal length, and $L_{F-{\rm TT}}$ the distance of the tip/tilt mirror to the AO focus. The impact offset δ on the tip/tilt mirror between the primary and secondary beams for a given separation α between primary and secondary targets is given by

$$\delta = \alpha F_{\rm tel}. \tag{A2}$$

The differential piston δOPD for a given tip/tilt mirror angle $\theta_{\rm TT}$ and a given impact offset δ is written as

$$\delta{\rm OPD} = 2\theta_{\rm TT}\delta. \tag{A3}$$

Altogether, the differential δOPD for a given separation α and wavefront tilt correction $\theta_{\rm Tilt}$ amounts to:

$$\frac{\delta{\rm OPD}}{\alpha\theta_{\rm Tilt}} = \frac{F_{\rm tel}^2}{L_{F-{\rm TT}}} = 528\,{\rm nm\,arcsec^{-2}}. \tag{A4}$$

As an illustration, the single-axis atmospheric tilt standard deviation $\sigma_{\Theta_{\rm Tilt}}$ is

$$\begin{aligned}\sigma_{\Theta_{\rm Tilt}} &= 0.427\,(D/r_0)^{5/6}\,(\lambda/D)\\ &= 0.112\,{\rm arcsec},\end{aligned} \tag{A5}$$

for a good Mauna Kea seeing $\lambda/r_0 = 0.5$ arcsec ($r_0 = 20.6$ cm), a telescope diameter $D = 10$ m, and a wavelength $\lambda = 500$ nm. Considering a typical separation of $\alpha = 15$ arcsec in this kind of seeing, the 2σ excursion of the differential δOPD is a significant $\pm 0.89\,\mu$m, per telescope.

Table 1
Parameters of the Keck AO Tip/Tilt Mirror Geometry

Parameter	Value	Unit
$F_{\rm tel}$	150.0	m
$L_{F-{\rm TT}}$	1.002	m
F to OAP1	1.860	m
OAP1 to DM	2.034	m
F plate scale	0.727	mm arcsec^{-1}

REFERENCES

Buscher, D. F. 1994, Proc. SPIE, 2200, 260
Colavita, M. M., Booth, A. J., Garcia-Gathright, J. I., et al. 2010, PASP, 122, 795
Colavita, M. M., Serabyn, E., Millan-Gabet, R., et al. 2009, PASP, 121, 1120
Colavita, M. M., Wallace, J. K., Hines, B. E., et al. 1999, ApJ, 510, 505
Colavita, M. M., Wizinowichet, P., Akeson, R. L., et al. 2013, PASP, 125, 1226
Daigne, G., & Lestrade, J.-F. 2003, A&A, 406, 1167
Delplancke, F. 2008, NewAR, 52, 199
Lane, B. F. 2003, PhD thesis, California Institute of Technology
Lane, B. F., & Colavita, M. M. 2003, AJ, 125, 1623
Lane, B. F., & Muterspaugh, M. W. 2004, ApJ, 601, 1129
Le Bouquin, J.-B., Bauvir, B., Haguenauer, P., et al. 2008, A&A, 481, 553
Le Mignant, D., van Dam, M. A., Bouchez, A. H., et al. 2006, Proc. SPIE, 6272, 627201
Mérand, A., Stefl, S., Bourget, P., et al. 2010, Proc. SPIE, 7734, 77340S
Millan-Gabet, R., Serabyn, E., Mennesson, B., et al. 2011, ApJ, 734, 67
Monnier, J. D., Pedretti, E., Thureau, N., et al. 2012, Proc. SPIE, 8445, 84450Y
Müller, A., Pott, J.-U., Morel, S., et al. 2010, Proc. SPIE, 7734, 773420
Pott, J.-U., Müller, A., Karovicova, I., & Delplancke, F. 2012, Proc. SPIE, 8445
Pott, J.-U., Woillez, J., Ragland, S., et al. 2010, ApJ, 721, 802
Ragland, S., Akeson, R. L., Armandroff, T., et al. 2009, ApJ, 703, 22

Rousset, G., Fontanella, J. C., Kern, P., Gigan, P., & Rigaut, F. 1990, A&A, 230, L29
Shao, M., & Colavita, M. M. 1992, A&A, 262, 353
Shao, M., & Staelin, D. H. 1980, ApOpt, 19, 1519
Wizinowich, P., Acton, D. S., Shelton, C., et al. 2000, PASP, 112, 315
Wizinowich, P. L. 2011, W. M. Keck Observatory News Letter—Summer 2011
Wizinowich, P. L., Le Mignant, D., Bouchez, A. H., et al. 2006, PASP, 118, 297
Woillez, J., Akeson, R., Colavita, M., et al. 2010, Proc. SPIE, 7734, 773412
Woillez, J., Akeson, R., Colavita, M., et al. 2012, PASP, 124, 51
Woillez, J., & Lacour, S. 2013, ApJ, 764, 109
Zhao, F., Diaz, R., Kuan, G. M., et al. 2003, Proc. SPIE, 4852, 370